Measurements of the branching fraction and decay distributions for $K_L \to \pi^\pm \mu^\mp \nu\gamma$ and $K_L \to \pi^\pm e^\mp \nu\gamma$

T. Alexopoulos,[11] T. Andre,[4] M. Arenton,[10] R. F. Barbosa,[7,*] A. R. Barker,[5,†] L. Bellantoni,[7] A. Bellavance,[9] E. Blucher,[4] G. J. Bock,[7] E. Cheu,[1] S. Childress,[7] R. Coleman,[7] M. D. Corcoran,[9] B. Cox,[10] A. R. Erwin,[11] R. Ford,[7] A. Glazov,[4] A. Golossanov,[10] J. Graham,[4] J. Hamm,[1] K. Hanagaki,[8] Y. B. Hsiung,[7] H. Huang,[5] V. Jejer,[10] D. A. Jensen,[7] R. Kessler,[4] H. G. E. Kobrak,[3] K. Kotera,[8] J. LaDue,[5] A. Ledovskoy,[10] P. L. McBride,[7] E. Monnier,[4,‡] K. S. Nelson,[10] H. Nguyen,[7] R. Niclasen,[5] V. Prasad,[4] X. R. Qi,[7] E. J. Ramberg,[7] R. E. Ray,[7] M. Ronquest,[10] E. Santos,[7,§] P. Shanahan,[7] J. Shields,[10] W. Slater,[2] D. Smith,[10] N. Solomey,[4] E. C. Swallow,[4,6] P. A. Toale,[5] R. Tschirhart,[7] Y. W. Wah,[4] J. Wang,[1] H. B. White,[7] J. Whitmore,[7] M. Wilking,[5] B. Winstein,[4] R. Winston,[4] E. T. Worcester,[4] T. Yamanaka,[8] and E. D. Zimmerman[5]

(The KTeV Collaboration)

[1]*University of Arizona, Tucson, Arizona 85721, USA*
[2]*University of California at Los Angeles, Los Angeles, California 90095, USA*
[3]*University of California at San Diego, La Jolla, California 92093, USA*
[4]*The Enrico Fermi Institute, The University of Chicago, Chicago, Illinois 60637, USA*
[5]*University of Colorado, Boulder, Colorado 80309, USA*
[6]*Elmhurst College, Elmhurst, Illinois 60126, USA*
[7]*Fermi National Accelerator Laboratory, Batavia, Illinois 60510, USA*
[8]*Osaka University, Toyonaka, Osaka 560-0043 Japan*
[9]*Rice University, Houston, Texas 77005, USA*
[10]*The Department of Physics and Institute of Nuclear and Particle Physics, University of Virginia, Charlottesville, Virginia 22901, USA*
[11]*University of Wisconsin, Madison, Wisconsin 53706, USA*

(Received 25 October 2004; published 12 January 2005)

We present measurements of $\mathcal{R}_{K\ell 3\gamma} \equiv \Gamma(K_L \to \pi^\pm \ell^\mp \nu\gamma; E^\star_\gamma > 10\ \text{MeV})/\Gamma(K_L \to \pi^\pm \ell^\mp \nu)$, where $\ell = \mu$ or e, and $E^\star_\gamma$ is the photon energy in the kaon rest frame. These measurements are based on K_L decays collected in 1997 by the KTeV (E832) experiment at Fermilab. With samples of 1385 $K_L \to \pi^\pm \mu^\mp \nu\gamma$ and 14221 $K_L \to \pi^\pm e^\mp \nu\gamma$ candidates, we find $\mathcal{R}_{K\mu 3\gamma} = (0.530 \pm 0.019)\%$ and $\mathcal{R}_{Ke3\gamma} = (4.942 \pm 0.062)\%$. We also examine distributions of photon energy and lepton-photon angle.

DOI: 10.1103/PhysRevD.71.012001 PACS numbers: 13.20.Eb, 14.40.Aq

I. INTRODUCTION

Radiative effects play an important role in relating the Cabibbo-Kobayashi-Maskawa (CKM) parameter $|V_{us}|$ to K_L semileptonic decays. Radiative effects enter the measurement of $|V_{us}|$ in two distinct ways. First, $|V_{us}|$ is extracted from the semileptonic decay rate $\Gamma_{K\ell 3} = \Gamma^{\text{Born}}_{K\ell 3} \times (1 + \delta_{\text{rad}})$, where $\ell = e$ or μ, $\Gamma^{\text{Born}}_{K\ell 3}$ is the Born-level decay rate proportional to $|V_{us}|^2$, and δ_{rad} describes radiative corrections. In our extraction of $|V_{us}|$ [1] $(1 + \delta_{\text{rad}}) = S_{EW}(1 + \delta^\ell_K)$, where S_{EW} is the short-distance radiative correction taken from [2], and the KLOR program [3] is used to determine δ^ℓ_K. The second role of radiative effects is in the Monte Carlo simulation (MC) that is used to determine the detector acceptance needed to measure the $K_{\ell 3}$ branching fractions and form factors. A Monte Carlo simulation requires a precise understanding of the kinematic distributions, particularly the photon energy spectrum and the angle between the charged lepton and photon. The sensitivity of the MC to radiative effects depends on the experimental technique. For the KTeV measurements [4,5], radiative effects in the simulation change the K_{e3} branching fraction by a few percent, and have a more significant impact on the form factors. The KLOR program that is used to determine δ^ℓ_K is also used to generate $K_L \to \pi^\pm \ell^\mp \nu(\gamma)$ decays in our Monte Carlo simulation, and to predict radiative semileptonic branching fractions.

To test our understanding of radiative semileptonic decays, we measure

$$\mathcal{R}_{K\ell 3\gamma} \equiv \frac{\Gamma(K_L \to \pi^\pm \ell^\mp \nu\gamma; E^\star_\gamma > 10\ \text{MeV})}{\Gamma(K_L \to \pi^\pm \ell^\mp \nu)}, \quad (1)$$

where $\ell = e$ or μ, and $E^\star_\gamma$ is the photon energy in the kaon rest frame. The denominator in Eq. (1) is the $K_{\ell 3}$ decay rate

*Permanent address: University of São Paulo, São Paulo, Brazil
†Deceased.
‡Permanent address: C.P.P. Marseille/C.N.R.S., France.
§Permanent address: University of São Paulo, São Paulo, Brazil.

which includes the emission of one or more radiated photons[1]. We also measure distributions of $E^\star_\gamma$ and the angle ($\theta^\star_{\gamma\ell}$) between the photon and charged lepton.

Previous $K_{\ell 3\gamma}$ analyses selected $E^\star_\gamma > 30$ MeV; for $K_{e3\gamma}$, an additional angular cut, $\theta^\star_{\gamma e} > 20^0$, was also required. In this analysis, we select events with $E^\star_\gamma >$ 10 MeV and remove the $\theta^\star_{\gamma\ell}$ requirement; these relaxed cuts allow us to study 5 times more radiated photons for $K_L \to \pi^\pm e^\mp \nu\gamma$, and 2.5 times more photons for $K_L \to \pi^\pm \mu^\mp \nu\gamma$.

The outline of this paper is as follows. Section II describes the theoretical treatment used to generate radiative effects in semileptonic decays. The KTeV apparatus is described in Sec. III, the $\mathcal{R}_{K\ell 3\gamma}$ analyses are presented in Sec. IV, and systematic uncertainties are discussed in Sec. V. Section VI describes the acceptance correction, as well as a correction from second-order radiative effects. Finally, results are presented in Sec. VII.

II. TREATMENT OF RADIATIVE DECAYS

In our Monte Carlo simulation, we use the KLOR program to generate both radiative and nonradiative $K_{\ell 3}$ events. KLOR models first-order radiative corrections to the $K_{\ell 3}$ decay mode using a phenomenological model [3,6,7]; below we give a brief description of this program. Second-order radiative effects are estimated using the PHOTOS program [8], and are discussed in Sec. VI B.

First-order radiative corrections are composed of both inner-bremsstrahlung (IB) and virtual contributions. Figure 1(g)–1(i) shows the IB contribution consisting of radiation from the pion, the charged lepton, and the vertex[2]. Data-MC comparisons of the kinematic distributions for radiated photons ($E^\star_\gamma$ and $\theta^\star_{\gamma\ell}$) are presented in Sec. VII C. Figure 1(a)–1(f) illustrates the virtual corrections that involve the emission and absorption of a photon by the pion, the charged lepton, or the effective vertex. The effects of virtual photon exchange are most prominent in the distributions of the pion-lepton mass ($m_{\pi\ell}$), and the transverse momentum of each charged particle (p_T). Using KLOR, data-MC comparisons in these distributions show good agreement (Fig. 3, 4 in [5]).

Radiative corrections to $K_{\ell 3}$ decays depend on the hadronic K–π form factors. The form factors depend on t, the square of the four-momentum transfer to the gauge boson ($W^\pm$). This four-momentum-squared is given by $t_1 = (p_\ell + p_\nu)^2$ when the photon is radiated from the pion, and by $t_2 = (p_K - p_\pi)^2$ when the photon is radiated from the charged lepton. Note that $t_1 = t_2$ without radiation, but differ when radiation is included. The t-dependence of the form factors is obtained from our measurements in [5].

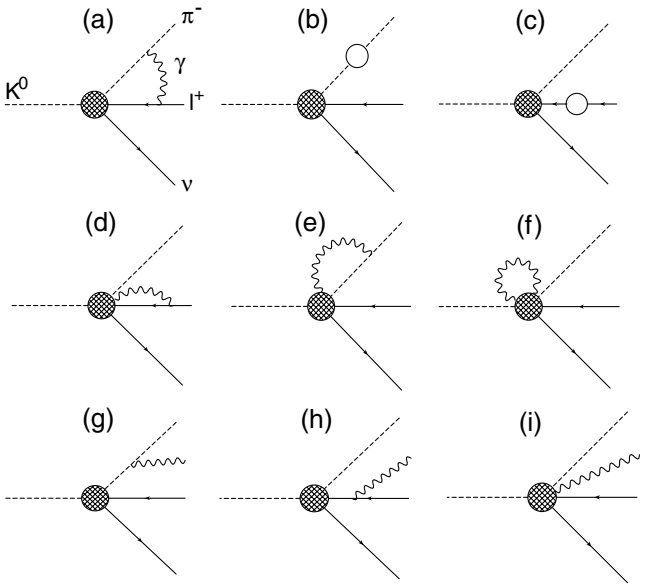

FIG. 1. Feynman diagrams for the first-order radiative corrections to the $K_{\ell 3}$ decay mode. Diagrams (a)–(f) are the virtual corrections while diagrams (g)–(i) are the inner-bremsstrahlung corrections. The open circles in diagram (b) and (c) denote the self-energy correction to the pion and lepton wave functions, respectively.

In the KLOR program, the virtual and inner-bremsstrahlung matrix elements are evaluated numerically. Numerical integration of the squared matrix elements over the phase space gives predictions for δ^ℓ_K, and also for the radiative branching fractions, $\mathcal{R}_{K\ell 3\gamma}$. The virtual matrix elements are integrated over three-body phase space, and the IB matrix elements are integrated over four-body phase space. Comparison of the predicted and measured radiative branching fractions are presented in Sec. VII. Note that the predictions from the KLOR program do not require any tuning from the data.

III. DETECTOR AND DATA COLLECTION

The KTeV detector has been described in detail elsewhere [9]. Here we give a brief description of the essential detector components. An 800 GeV proton beam incident on a beryllium-oxide target produces neutral kaons. A collimation system results in two parallel neutral beams beginning 90 meters from the beryllium target; each beam consists of roughly equal numbers of kaons and neutrons. The fiducial decay region is 123–158 meters from the target, and the vacuum region extends from 20–159 meters.

The KTeV detector (Fig. 2) is located downstream of the decay region. A spectrometer consisting of four drift cham-

[1] $K_{\ell 3}$ refers to semileptonic decays including radiation; $K_{\ell 3\gamma}$ refers to radiative $K_L \to \pi^\pm \ell^\mp \nu\gamma$ in which the photon energy is above the analysis threshold of 10 or 30 MeV.

[2] Radiation from the vertex is required to preserve gauge invariance.

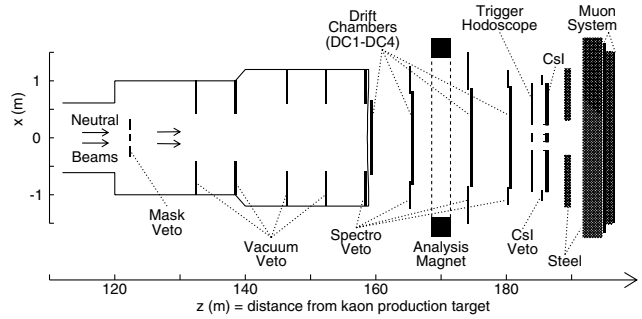

FIG. 2. Plan view of the KTeV (E832) detector. The evacuated decay volume ends with a thin vacuum window at $Z = 159$ m. K_L decays from the two neutral beams are the source of semileptonic decays.

bers, two upstream and two downstream of a dipole magnet, measures the momentum of charged particles; the resolution is $\sigma_p/p \simeq [1.7 \oplus (p/14)] \times 10^{-3}$, where p is the track momentum in GeV/c. Downstream of the spectrometer lies a scintillator "trigger hodoscope," which is used to trigger on charged particles. Farther downstream there is an electromagnetic calorimeter made of 3100 pure Cesium Iodide (CsI) crystals [see Fig. (3)]. For photons and electrons, the energy resolution is better than 1% and the position resolution is about one mm. The CsI calorimeter has two holes to allow the neutral beams to pass through without interacting. Two scintillator "muon hodoscopes," behind four and 5 meters of steel, are used to detect muons. The downstream muon hodoscope consists of horizontal (MUH) and vertical (MUV) counters, each with 15 cm segmentation. Eight photon-veto detectors along the decay region and spectrometer reject events with escaping particles. The trigger for both semileptonic decay modes requires a few hits in the drift chambers upstream of the magnet, and at least two hits in the trigger hodoscope.

A Monte Carlo simulation is used to determine the acceptance for the $K_{\ell 3}$ and $K_{\ell 3\gamma}$ decay modes. KLOR is used to generate semileptonic decays as discussed in Sec. II. For the generation of inner-bremsstrahlung with KLOR, the photon energy cutoff in the kaon rest frame is 3.5 keV. This cutoff results in a minimum lab photon energy of a few hundred keV, which is below the energy for which photons affect the detector acceptance. The fraction of $K_{\ell 3}$ decays with a photon above the 3.5 keV cutoff is 21% for K_{e3}, and 3.7% for $K_{\mu 3}$.

Each of the decay products (pion, lepton, photon) is traced through the detector, including the effects of multiple scattering, energy loss from ionization, bremsstrahlung for electrons, e^+e^- pair-production for photons, secondary decays for pions, and pions that interact hadronically in the detector. The effects of accidental activity are included by overlaying events from a trigger that recorded random activity in the detector that is proportional to the instantaneous intensity of the proton beam.

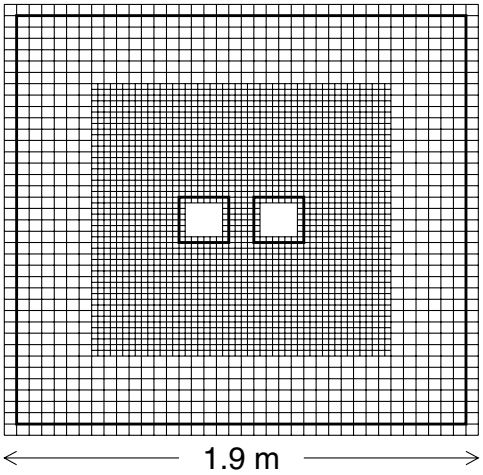

FIG. 3. Layout of CsI calorimeter. The small crystals (inner region) have dimension $2.5 \times 2.5 \times 50$ cm^3; the large crystals (outer region) have dimension $5.0 \times 5.0 \times 50$ cm^3. The two neutral beams go through the beam holes (into page) shown by the two inner squares. The fiducial cut, indicated by the dark lines, excludes radiated photons that hit a crystal near the beam holes or near the outer boundary.

In addition to detailed tracing of the decay products, the KTeV MC also treats the detector response in great detail, particularly the drift chamber inefficiencies and detector resolutions. A detailed discussion of the simulation is given in [9].

The semileptonic samples presented here were collected during a oneday run in 1997 in which the incident proton beam intensity was reduced to 10% of the nominal intensity used to measure ϵ'/ϵ [9]. The regenerator, which was used to generate K_S in the ϵ'/ϵ measurement, was removed from the beamline resulting in two K_L beams. Note that this low-intensity sample is the same as that used for the $K_{\ell 3}$ form-factor measurements [5].

IV. ANALYSIS

The analysis strategy is first to identify a $K_{\ell 3}$ decay (Sec. IVA), and then search for an extra photon in the CsI calorimeter (Sec. IV B). The photon selection is optimized to reduce background from semileptonic events with a fake-photon cluster, and also from other K_L decays (mainly $K_L \to \pi^+\pi^-\pi^0$) which are misidentified as $K_{\ell 3\gamma}$. Kinematic requirements on the pion-lepton system for $K_{\ell 3}$ candidates are also applied to the pion-lepton-photon system for $K_{\ell 3\gamma}$ candidates.

A. $K_L \to \pi^\pm \ell^\mp \nu$ Selection

The first step in the semileptonic decay reconstruction is to identify the charged pion and lepton. The spectrometer is used to find two charged tracks. For each track, the momentum is required to be above 8 GeV/c, and a cluster in the CsI calorimeter is required to be near the track

projection at the CsI. If the cluster energy (E) divided by the track momentum (p) is greater than 0.92, the track is identified as an electron; this cut retains 99.8% of the electrons and rejects 99.5% of the pions. If the corresponding E/p value is less than 0.85, and the track does not point to a hit muon counter, the track is identified as a pion; this cut retains 99.1% of the pions and rejects 99.93% of the electrons. A muon track candidate must have momentum above 10 GeV/c, point near a hit counter in both MUH and MUV[3], and be matched to a CsI cluster with energy less than 2 GeV (5 times the average energy deposit). Events consisting of either "$\pi\mu$" or "πe" candidates are selected. Note that πe candidates are vetoed by activity in the muon hodoscopes.

After particle identification, but before kinematic requirements, there is a small background from $K_L \to \pi^+\pi^-\pi^0$ ($\mathrm{K}_{3\pi}$) decays in which the π^0-photons do not fire a photon veto, and a pion either decays or is misidentified as an electron. At this intermediate stage of the analysis, the $\mathrm{K}_{3\pi}$ background is 0.5% in the $\pi\mu$ ($\mathrm{K}_{\mu 3}$) sample and 0.1% in the πe (K_{e3}) sample. When a radiated photon cluster is required in the CsI calorimeter (see below), the $\mathrm{K}_{3\pi}$ background increases significantly: 67% background in the $K_{\mu 3\gamma}$ sample, and almost 10% in the $K_{e3\gamma}$ sample. To suppress $K_{3\pi}$ background, a kinematic variable is used which distinguishes decays with a missing π^0 from decays with a missing neutrino[4]; we require $\mathrm{k}_{+-0} < -0.00625$ for the πe sample, and $\mathrm{k}_{+-0} < -0.01$ for the $\pi\mu$ sample.

For reconstructed $K_{\ell 3}$ decays with a missing neutrino, there is a twofold ambiguity in determining the kaon energy (E_K). Both E_K solutions are required to satisfy the 40–160 GeV range for which the energy spectrum is well-measured[5]. For reconstructed decays in which the true kaon energy is between 40 and 160 GeV, 20% of these events are rejected by the requirement on both kaon energy solutions.

After these selection requirements, there are 1 691 400 $\mathrm{K}_{\mu 3}$ and 2 191 077 K_{e3} candidates. The background in each $K_{\ell 3}$ mode is $\sim 10^{-4}$, and is ignored.

B. $\mathrm{K_L} \to \pi^\pm \ell^\mp \nu\gamma$ Selection

After finding a pion and lepton track that satisfy kinematics for either of the $K_{\ell 3}$ decays, we search for a photon in the CsI calorimeter. A candidate radiated photon from a $\mathrm{K_L} \to \pi^\pm \ell^\mp \nu\gamma$ decay is a single CsI cluster with energy above 3 GeV and a transverse profile consistent with a photon (Appendix A). To have a well-defined acceptance, the photon position must not lie in a crystal adjacent to the beam-hole, and must also lie away from the outer edge of the calorimeter (Fig. 3). To avoid overlapping clusters in the CsI, the photon cluster is required to be at least 20 cm from the lepton and at least 40 cm from the pion.

As with $K_{\ell 3}$ decays, $K_{\ell 3\gamma}$ decays have two kaon energy solutions, both of which must pass the 40–160 GeV requirement. Similarly, both $\mathrm{E}^\star_\gamma$ solutions must be above 10 MeV. For both $K_{\ell 3}$ and $K_{\ell 3\gamma}$, the square of the reconstructed neutrino momentum is required to be greater than zero.

After finding a single-photon cluster in the CsI, there is background from $\mathrm{K_L} \to \pi^+\pi^-\pi^0$ decays, and from $K_{\ell 3}$ decays with a fake-photon cluster; methods to reduce these backgrounds are described below. Kaon decays other than $\mathrm{K_L} \to \pi^+\pi^-\pi^0$ contribute negligible background.

1. *Background from misidentified K_L decays*

Background from $K_L \to \pi^+\pi^-\pi^0$ decays arises when one of the π^0 photons is not detected, and a charged pion either decays or is misidentified as an electron. As discussed in Sec. IV A, this $\mathrm{K}_{3\pi}$ background is suppressed by the k_{+-0} requirement. Figure 4 shows the k_{+-0} distribution for both $K_{\ell 3\gamma}$ samples; after the k_{+-0} requirement, the $K_{3\pi}$ background is $(4.39 \pm 1.75)\%$ in the $K_{\mu 3\gamma}$ sample, and less than 0.01% in the $K_{e3\gamma}$ sample. The 40% relative uncer-

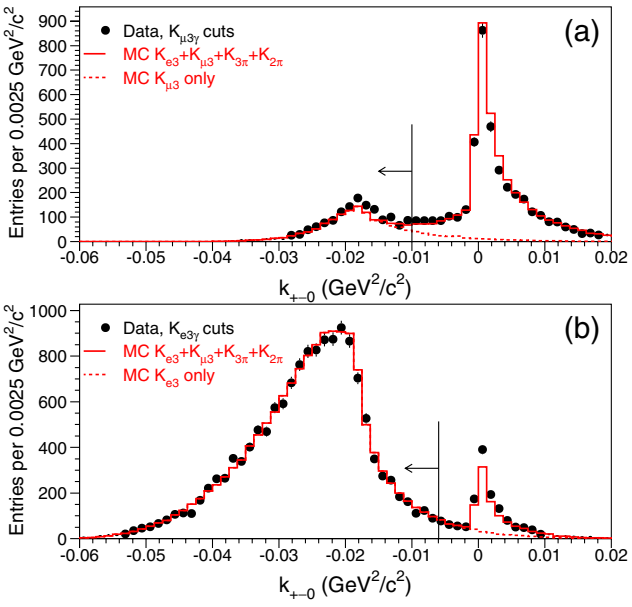

FIG. 4 (color online). k_{+-0} distribution for (a) $K_{\mu 3\gamma}$, and (b) $K_{e3\gamma}$. Arrows indicate selected events for the $K_{\ell 3\gamma}$ samples. Each peak at $\mathrm{k}_{+-0} \sim 0$ is background from $K_L \to \pi^+\pi^-\pi^0$ decays.

[3]For the track projection to the 15×15 cm^2 hit region of MUH and MUV, the proximity requirement is based on the amount of multiple scattering and is momentum dependent.

[4]For $K_L \to \pi^+\pi^-\pi^0$ decays, the kinematic variable k_{+-0} is the longitudinal π^0 momentum-squared in a frame in which the $\pi^+\pi^-$ momentum is orthogonal to the kaon momentum. See [4] for more details.

[5]If there were no E_K requirement, or a requirement only on the most probable E_K solution, the analysis would accept decays with kaon energy outside the well-measured 40–160 GeV range, and thereby degrade the acceptance determination.

tainty in the $K_{3\pi}$ background is based on the data-MC discrepancy in the background region shown in Fig. 4(b).

Backgrounds from other kaon decays (K_{e4} and $\pi^+\pi^-\gamma$) are simulated and normalized according to their branching fractions. Since there is no measurement or upper limit for $K_L \to \pi^0\pi^\pm\mu^\mp\nu$, we searched for this mode (Appendix B) and set an upper limit on the branching fraction of $B(K_L \to \pi^0\pi^\pm\mu^\mp\nu) < 2 \times 10^{-5}$.

2. Background from $K_{\ell 3}$ with fake photon

The other significant background is from $K_L \to \pi^\pm\ell^\mp\nu+$ "fake photon." Fake-photon clusters can come from (1) π-hadron interactions in the detector, (2) accidentals, and (3) external bremsstrahlung upstream of the magnet. For each fake-photon source, the following subsections describe additional analysis requirements to reduce these backgrounds; background-to-signal ratios are determined with the MC.

Pion hadron interactions—If a π-hadron interaction leaves a fake-photon candidate, there are usually additional clusters in the CsI calorimeter with transverse profiles inconsistent with a photon. We therefore veto events that have an extra CsI cluster with energy above 1 GeV, and a transverse profile inconsistent with a photon. To avoid vetoing on satellite clusters from the pion shower in the CsI, we veto an event only if the extra cluster lies at least 30 cm away from the pion. This extra cluster veto is required in both the $K_{\ell 3}$ and $K_{\ell 3\gamma}$ samples.

The π-hadron interaction background is reduced further by requiring the photon cluster candidate to lie at least 40 cm away from the pion at the CsI. The background level is $(1.60 \pm 0.32)\%$ for $K_{\mu 3\gamma}$, and $(0.54 \pm 0.11)\%$ for $K_{e3\gamma}$. The uncertainty on this background is explained in Appendix C.

Accidental cluster—To prevent an accidental cluster from faking a radiative photon, we use the energy-vs-time profiles recorded by the CsI calorimeter. For each radiated photon candidate, the CsI cluster energy deposited before the event must be consistent with pedestal, and the energy deposited in the first RF bucket[6] must be well above pedestal (Fig. 5). These two requirements on the energy-vs-time profile reduce the accidental background by a factor of 10, resulting in accidental background contributions of $(1.68 \pm 0.89)\%$ for $K_{\mu 3\gamma}$, and $(0.22 \pm 0.11)\%$ for $K_{e3\gamma}$. The relatively large error on the accidental background is because of the low statistics of the accidental event sample used to include accidental activity in the MC.

External bremsstrahlung (K_{e3} *only*): A photon from external bremsstrahlung upstream of the magnet is separated from the electron at the CsI calorimeter, and is therefore a source of fake-photon clusters. Note that external bremsstrahlung downstream of the magnet results in a photon that lies on top of the electron at the CsI calorimeter, and therefore does not result in background. To remove events with a photon produced by external bremsstrahlung upstream of the magnet (which would fake $K_{e3\gamma}$ with $\theta^\star_{\gamma e} \sim 0^0$), the photon candidate is required to be at least 2 cm away from the CsI position corresponding to the electron track projection from upstream of the magnet [see $\Delta R_{\gamma-\mathrm{brem}}$ in Fig. 6]. This background is $(0.20 \pm 0.02)\%$.

[6]The proton beam has a 53 MHz micro-structure such that protons (and hence neutral kaons) arrive in 1 ns wide radio-frequency (RF) buckets, in 19 ns intervals. The CsI integration time is six RF buckets.

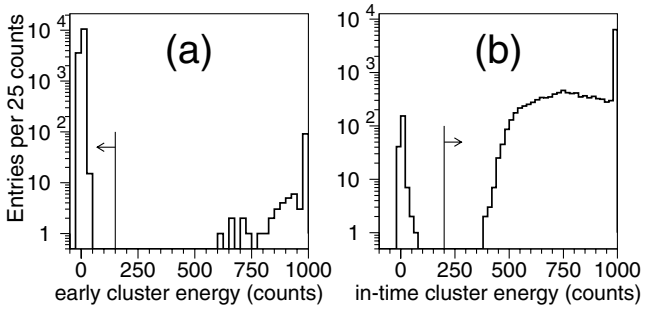

FIG. 5. For radiated photon cluster candidates in the $K_{e3\gamma}$ sample, (a) cluster-energy deposit in RF bucket prior to event, and (b) cluster-energy deposit in first RF bucket. Energy is shown as analog-to-digital converter (ADC) counts (1 ADC count is about 1 MeV). The arrow in each plot indicates the selected region.

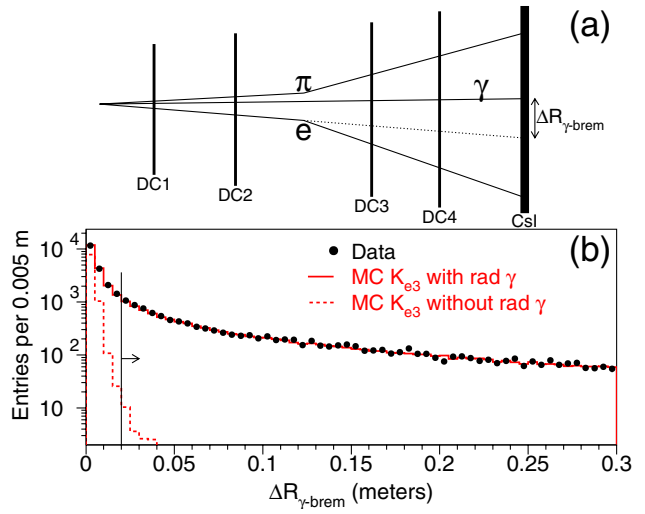

FIG. 6 (color online). (a) Top view of spectrometer (DC1-4) and CsI calorimeter, and overlay of $K_{e3\gamma}$ decay. $\Delta R_{\gamma-\mathrm{brem}}$ is the distance between the photon candidate at the CsI and the location of the electron track projected from upstream of the magnet (dotted line); the latter is where a photon from external bremsstrahlung would hit the CsI. (b) $\Delta R_{\gamma-\mathrm{brem}}$ distribution for data (dots), for MC with radiated photons (histogram) and for MC without radiated photons (dashed histogram). Plots are shown after $K_{e3\gamma}$ requirements. The arrow indicates the analysis selection.

TABLE I. The background-to-signal ratio (B/S) for each background component.

Background process	$K_{\mu 3\gamma}$ B/S (%)	$K_{e3\gamma}$ B/S (%)
$K_{\ell 3}$ + π-hadron interaction	(1.60 ± 0.32)	(0.54 ± 0.11)
$K_{\ell 3}$ + accidental cluster	(1.68 ± 0.89)	(0.22 ± 0.11)
$K_{\ell 3}$+ external bremsstrahlung	—	(0.20 ± 0.02)
K_{e3} + particle misidentified	(0.06 ± 0.02)	—
$K_{\mu 3}$+ particle misidentified	—	<0.01
$K_L \to \pi^+\pi^-\pi^0$	(4.39 ± 1.75)	<0.01
$K_{L,S} \to \pi^+\pi^-\gamma$	(0.19 ± 0.08)	<0.01
$K_L \to \pi^0\pi^\pm e^\mp\nu$	—	(0.07 ± 0.03)
$K_L \to \pi^0\pi^\pm\mu^\mp\nu$	<0.05	—
Total	$(7.91 \pm 1.99)\%$	$(1.04 \pm 0.16)\%$

Background summary: The backgrounds for both $K_{\ell 3\gamma}$ modes are summarized in Table I. The total background level is $(7.91 \pm 1.99)\%$ for $K_{\mu 3\gamma}$ and $(1.04 \pm 0.16)\%$ for $K_{e3\gamma}$. Figs. 7 and 8 show $E^\star_\gamma$ and $\cos(\theta^\star_{\gamma\ell})$ distributions for the $K_{\mu 3\gamma}$ and $K_{e3\gamma}$ decay modes, respectively. In these plots, the data points correspond to the distributions before background subtraction, and the dotted histograms show the background prediction. The final $K_{\ell 3\gamma}$ samples are obtained after subtracting background coming from other kaon decays. The three $K_{\ell 3}$+ fake-photon backgrounds are not subtracted from data since these effects are included in the signal MC. After analysis selection and background subtraction, there are 1385 $K_{\mu 3\gamma}$ and 14221 $K_{e3\gamma}$ candidates.

V. SYSTEMATIC UNCERTAINTIES

The $K_{\ell 3\gamma}/K_{\ell 3}$ ratios are insensitive to the small inefficiencies related to track-finding and particle identification. The main sources of systematic uncertainty are related to

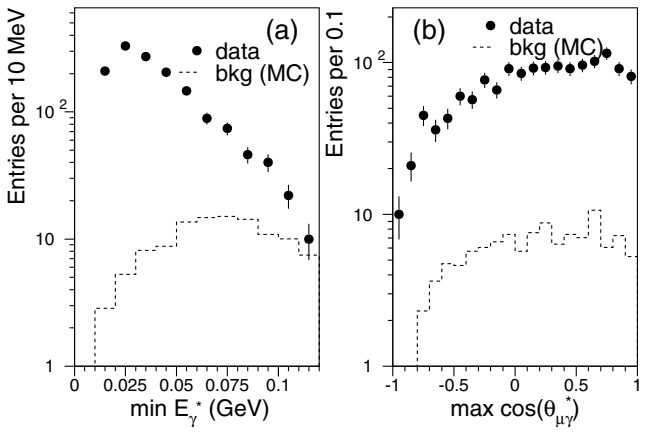

FIG. 7. For $K_L \to \pi^\pm\mu^\mp\nu\gamma$ candidates without background subtraction, (a) minimum $E^\star_\gamma$ and (b) maximum $\cos(\theta^\star_{\gamma e})$ for the two kinematic solutions. Dots are data, and dashed histogram is the background predicted by the MC.

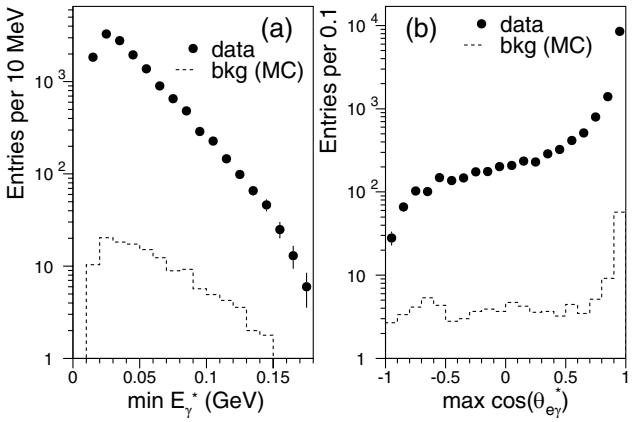

FIG. 8. For $K_L \to \pi^\pm e^\mp\nu\gamma$ candidates without background subtraction, (a) minimum $E^\star_\gamma$ and (b) maximum $\cos(\theta^\star_{\gamma e})$ for the two kinematic solutions. Dots are data, and dashed histogram is the background predicted by the MC.

$K_{\ell 3\gamma}$ background, the efficiency of reconstructing a radiated photon, and the aperture for photons. These systematic uncertainties are discussed below.

Background: For $\mathcal{R}_{K\mu 3\gamma}$, the background contributes 1.99% uncertainty, mostly from $K_L \to \pi^+\pi^-\pi^0$ decays; for $\mathcal{R}_{Ke3\gamma}$ the corresponding uncertainty is 0.16%, mainly from K_{e3} with a false photon cluster.

Extra cluster veto: Removing the extra cluster veto requirement changes $\mathcal{R}_{K\mu 3\gamma}$ by -0.60% and changes $\mathcal{R}_{Ke3\gamma}$ by $+0.58\%$; these changes are included as uncertainties in $\mathcal{R}_{K\ell 3\gamma}$.

CsI energy scale: The CsI energy scale is calibrated to better than 0.1%, and results in a 0.1% uncertainty for both $\mathcal{R}_{K\ell 3\gamma}$ ratios.

Photon aperture and beamline material: The beam-hole aperture is studied with electrons from K_{e3} decays. The effective size is known to $\pm 200\mu$m, leading to a 0.1% uncertainty for both $\mathcal{R}_{K\ell 3\gamma}$ ratios. The same 200μm uncertainty affects the $\Delta R_{\gamma-\text{brem}}$ requirement, resulting in a 0.30% uncertainty in $\mathcal{R}_{Ke3\gamma}$, and less than 0.01% uncertainty in $\mathcal{R}_{K\mu 3\gamma}$.

Photon inefficiency: Three sources of photon inefficiency are considered: $\gamma \to e^+e^-$ conversions in detector material, CsI readout, and the transverse profile requirement. A photon traverses 4% of a radiation length through the KTeV detector before reaching the CsI calorimeter, and this results in a 1% reconstruction loss for the radiated photon. Based on the data-MC agreement in the first two bins of Fig. 6, the amount of material is known to better than 10%, resulting in a systematic uncertainty of 0.1% on $\mathcal{R}_{K\ell 3\gamma}$. The CsI readout efficiency is studied with events in which light from a laser is distributed to each crystal via 3100 fibers, and muons are used to check dead material (wrapping) between the crystals; this results in a 0.01% uncertainty. The inefficiency of the transverse profile requirement is discussed in Appendix A, resulting in a

systematic uncertainty of 0.2% for $K_{e3\gamma}$, and 0.06% for $K_{\mu 3\gamma}$.

Muon hodoscope efficiency: In the MC, if muon scattering in the steel is turned off and gaps between the muon system counters are ignored, $\mathcal{R}_{K\mu 3\gamma}$ changes by 2%. Using the nominal MC that includes scattering and gaps, we compare data and MC distributions of the distance between the track extrapolation and the hit muon system counters; this comparison shows that muon propagation through the steel is described to better than 20% precision, leading to a systematic uncertainty of 0.4% on $\mathcal{R}_{K\mu 3\gamma}$.

Pion punchthrough to muon hodoscope: Hadronic pion interactions downstream of the CsI calorimeter may result in activity in the muon hodoscopes. For K_{e3} decays, any activity in the muon system results in a veto. For $K_{\mu 3}$ decays, pion punchthrough resulting in a second hit in the muon hodoscope results in a veto. $K_L \to \pi^+\pi^-\pi^0$ decays are used to measure the probability for a pion to give a signal in the muon hodoscope; this probability is $(1.0 \pm 0.1) \times 10^{-4} p_\pi$, where p_π is the pion momentum in GeV/c. The systematic uncertainty is based on the difference in the average pion momentum between $K_{\ell 3}$ and $K_{\ell 3\gamma}$ decays. This momentum difference is 0.3 GeV/c for K_{e3}, resulting in a 0.003% uncertainty on $\mathcal{R}_{Ke3\gamma}$, and 3 GeV/c for $K_{\mu 3}$, resulting in a 0.03% uncertainty on $\mathcal{R}_{K\mu 3\gamma}$.

Radiative effects and form factors in matrix element: As discussed in Sec. VI B, the uncertainty in radiative effects is from second-order radiative correction; this leads to 0.5% uncertainty in $\mathcal{R}_{K\ell 3\gamma}$. The correction from more than two radiated photons is roughly $0.02^2 = 0.0004$, which is much smaller than the uncertainty on second-order corrections. Variations in the form factors measured by KTeV [5] lead to 0.1% uncertainty on $\mathcal{R}_{K\ell 3\gamma}$.

TABLE II. Summary of systematic and statistical uncertainties. The total uncertainty in the last row is the sum (in quadrature) of the systematic and statistical uncertainties.

Source of Uncertainty	% Uncertainty for: $\mathcal{R}_{\mathrm{K}\mu 3\gamma}$	$\mathcal{R}_{\mathrm{Ke}3\gamma}$
Background	1.99	0.16
Extra cluster veto	0.60	0.58
CsI energy scale	0.10	0.08
γ beam-hole aperture	0.09	0.09
$\Delta R_{\gamma-\mathrm{brem}}$	<0.01	0.30
Photon inefficiency	0.12	0.22
Muon hodoscope inefficiency	0.4	–
Pion punchthrough to muon hodoscope	0.03	0.003
Form factors	0.1	0.1
$n_\gamma \geq 2$ rad corrections	0.5	0.5
MC signal statistics	0.89	0.28
Total systematic	2.36%	0.92%
Data statistics	2.69%	0.84%
Total uncertainty	3.58%	1.25%

The uncertainties are summarized in Table II. The total systematic uncertainty is 2.36% for $\mathcal{R}_{\mathrm{K}\mu 3\gamma}$, and 0.92% for $\mathcal{R}_{\mathrm{Ke}3\gamma}$. These systematic uncertainties are comparable to the statistical uncertainties.

VI. EXTRACTION OF RESULTS

A. Acceptance corrections

The relative branching fraction for radiative semileptonic decays is determined from the data and MC acceptance corrections by

$$\mathcal{R}_{\mathrm{K}\ell 3\gamma} = \frac{N^{\mathrm{data}}_{K\ell 3\gamma}/A_{K\ell 3\gamma}}{N^{\mathrm{data}}_{K\ell 3}/A_{K\ell 3}}, \tag{2}$$

where $N^{\mathrm{data}}_{\mathrm{mode}}$ is the number of reconstructed decays in data, and A_{mode} is the acceptance determined by the Monte Carlo simulation. Note that the subscript mode refers to either $\mathrm{K}_{\ell 3}$ or $\mathrm{K}_{\ell 3\gamma}$. The acceptance for each mode is defined as

$$A_{\mathrm{mode}} = N^{MCrec}_{\mathrm{mode}}/N^{MCgen}_{\mathrm{mode}}, \tag{3}$$

where $N^{MCgen}_{\mathrm{mode}}$ and $N^{MCrec}_{\mathrm{mode}}$ are the numbers of generated and reconstructed events, respectively. $N^{MCgen}_{K\ell 3}$ is the number of generated $\mathrm{K_L} \to \pi^\pm \ell^\mp \nu(\gamma)$ events in which the generated kaon energy and decay vertex are within the nominal ranges (40–160 GeV/c and 123–158 m). $N^{MCgen}_{K\ell 3\gamma}$ is the number of generated $\mathrm{K_L} \to \pi^\pm \ell^\mp \nu\gamma$ events with a radiated photon energy greater than 10 MeV, and with the same energy and vertex requirements as for $N^{MCgen}_{K\ell 3}$. For each sample of generated $K_{\ell 3}$ and $K_{\ell 3\gamma}$ events, $N^{MCrec}_{K\ell 3}$ and $N^{MCrec}_{K\ell 3\gamma}$ are the numbers of events that satisfy the selection requirements in Sec. IV. The approximate acceptance is 20% for $K_{\ell 3}$ decays and 3% for $K_{\ell 3\gamma}$ decays. For $K_{e3\gamma}$, the acceptance is corrected for second-order radiative effects as described below.

B. Second-order radiative corrections

First-order radiative effects in $K_{\ell 3}$ decays are fully treated as described in Sec. II. The precision of this analysis, however, requires a correction from second-order radiative effects involving two radiated photons. With two radiated photons, the definition of $\mathcal{R}_{K\ell 3\gamma}$ is modified to include semileptonic decays with at least one photon above 10 MeV. To see why second-order radiative effects are needed, consider the $K_L \to \pi^\pm e^\mp \nu$ acceptance. The MC with first-order radiative effects changes the acceptance by 2.5% compared to the Born-level (zero order) MC without radiative effects. This correction suggests that to determine the acceptance for radiative $\mathrm{K_L} \to \pi^\pm \mathrm{e}^\mp \nu\gamma$ (first order), there is a few percent acceptance correction from the next (second) order in radiative corrections. Note that this dependence on higher order radiative effects depends on the experimental apparatus. The KTeV sensitivity is largely

from the kinematic selection and the hermetic veto system with low thresholds (150 MeV).

The second-order radiative correction to the acceptance is estimated using PHOTOS [8], which allows for up to two radiated photons. We begin by generating MC with single-photon radiation from PHOTOS, and then reweight PHOTOS to match data distributions in the variables $E^\star_\gamma$ and $\theta^\star_{\gamma\ell}$[7]. For two-photon generation with PHOTOS, the reweighting is applied to the higher energy photon. The correction to the radiative acceptance for second-order effects is given by

$$A_{\gamma\gamma/\gamma} \equiv A_{\mathrm{PHOTOS}-2\gamma}/A_{\mathrm{PHOTOS}-1\gamma}, \tag{4}$$

where $A_{\mathrm{PHOTOS}-1,2\gamma}$ is the acceptance determined with PHOTOS using the option to allow up to one or two radiated photons. The final acceptance ($A_{K\ell 3\gamma}$) is given by $A_{\gamma\gamma/\gamma}$ times the acceptance determined from the MC using KLOR [3].

Evidence for a second radiated photon is seen in the photon candidate multiplicity in the CsI calorimeter. The photon multiplicity is checked for $K_{\ell 3}$ candidates after requiring all photon identification requirements (cluster energy greater than 3 GeV, transverse shape, etc.), but before $K_{\ell 3\gamma}$ kinematics are applied. The fraction of these events with two-photon candidates ($\eta_{\gamma\gamma}$) is $\eta_{\gamma\gamma} = (0.39 \pm 0.05)\%$ in data. In our MC using the KLOR generator, events with two-photon candidates are mostly from accidentals, and $\eta_{\gamma\gamma} = (0.17 \pm 0.01)\%$. For MC using PHOTOS with one radiated photon, $\eta_{\gamma\gamma} = (0.18 \pm 0.01)\%$. These MC generators (KLOR and PHOTOS) agree with each other, but disagree with the data. For MC using PHOTOS with two radiated photons, $\eta_{\gamma\gamma} = (0.36 \pm 0.02)\%$; this good agreement with data shows that PHOTOS provides a reasonable second-order correction to the acceptance.

For $K_L \to \pi^\pm e^\mp \nu\gamma$, $A_{\gamma\gamma/\gamma} = 0.982 \pm 0.005$[8], where the uncertainty comes from the limited statistics in the data-MC comparison of events with two-photon candidates. For $K_L \to \pi^\pm \mu^\mp \nu\gamma$, the two-photon candidates are consistent with accidentals, and $A_{\gamma\gamma/\gamma}$ is consistent with one. We therefore set $A_{\gamma\gamma/\gamma} = 1.0$ for $K_L \to \pi^\pm \mu^\mp \nu$, but include an additional 0.5% uncertainty on $\mathcal{R}_{K\mu 3\gamma}$.

[7]PHOTOS without reweighting agrees with data in the $E^\star_\gamma$ variable, but has a large disagreement in the $\theta^\star_{\gamma\ell}$ distribution. See Appendix C of [3] for discussion of PHOTOS.

[8]This 1.8% second-order acceptance correction is much larger than the 0.2% probability of observing a second radiative photon in the CsI calorimeter. The 3 GeV minimum cluster-energy requirement severely limits the chance of observing a second radiated photon, while radiated photons with much less energy effect the acceptance.

VII. RESULTS

A. $K_L \to \pi^\pm \mu^\mp \nu\gamma$ branching fraction

For the muonic semileptonic decay mode, the radiative branching fraction is

$$\begin{aligned}\mathcal{R}_{K\mu 3\gamma}(E^\star_\gamma > 10\ \mathrm{MeV}) &= [0.530 \pm 0.014(\mathrm{stat}) \\ &\quad \pm 0.012(\mathrm{syst})]\% \\ &= [0.530 \pm 0.019]\%. \end{aligned} \tag{5}$$

The only previous measurement of this radiative mode [10] required $E^\star_\gamma > 30$ MeV. To compare with this measurement, we have also applied a 30 MeV requirement on the photon energy; the results are

$$\mathcal{R}_{K\mu 3\gamma}(\mathrm{KTeV}; E^\star_\gamma > 30\ \mathrm{MeV}) = [0.209 \pm 0.009]\% \tag{6}$$

$$\mathcal{R}_{K\mu 3\gamma}(\mathrm{NA48}; E^\star_\gamma > 30\ \mathrm{MeV}) = [0.208 \pm 0.026]\% \tag{7}$$

which are in good agreement. The KTeV result is almost 3 times more precise than the previous measurement. Figure 9 compares our measurement of $\mathcal{R}_{K\mu 3\gamma}$ with NA48, and with the predictions from Andre [3] and FFS [6]. These comparisons show good agreement between the measurements and theory predictions. Table III summarizes the $\mathcal{R}_{K\mu 3\gamma}$ results from KTeV and the predictions from KLOR.

B. $K_L \to \pi^\pm e^\mp \nu\gamma$ branching fraction

For the electronic semileptonic decay mode, the branching fraction is

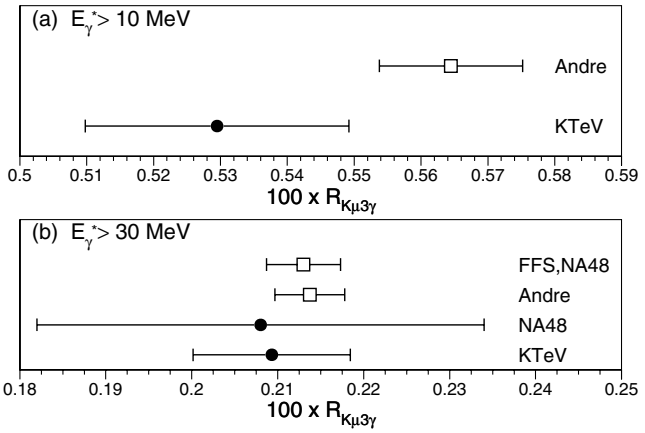

FIG. 9. Comparison of $\mathcal{R}_{K\mu 3\gamma}$ among experiment and theory for (a) $E^\star_\gamma > 10$ MeV, and (b) $E^\star_\gamma > 30$ MeV. The experimental results are from KTeV and NA48 [10]. The theory predictions are from Andre [3] and from Fearing, Fischbach, and Smith, FFS [6]. The FFS prediction is determined by NA48, and is corrected by $(1 + \delta^\mu_K)^{-1}$ [3]. The theory uncertainties are taken to be $\delta^\mu_K = 0.019$ times the prediction.

TABLE III. Summary of $\mathcal{R}_{K\mu 3\gamma}$ values measured by KTeV and predicted by KLOR.

Min $E^{\star}_{\gamma}$ (MeV)	Min $\theta^{\star}_{\gamma\mu}$ (Degree)	KTeV Result (%)	KLOR Prediction (%)	KTeV/KLOR Ratio
10	0	0.530 ± 0.019	0.564 ± 0.011	0.938 ± 0.038
30	0	0.209 ± 0.009	0.214 ± 0.004	0.979 ± 0.046

$$\mathcal{R}_{\mathrm{Ke3}\gamma}(\mathrm{E}^{\star}_{\gamma} > 10\ \mathrm{MeV}) = [4.942 \pm 0.042(\mathrm{stat}) \pm 0.046(\mathrm{syst})]\% = [4.942 \pm 0.062]\%. \quad (8)$$

Figure 10(a) compares our measurement of $\mathcal{R}_{Ke3\gamma}$ with NA31, and with several theory predictions. The measurements and predictions show good agreement, except for the PHOTOS prediction. Although the PHOTOS prediction is not consistent with the measurements, it provides the only estimate on the impact of second-order radiative effects; PHOTOS suggests that second-order effects lower the predicted value of $\mathcal{R}_{Ke3\gamma}$ by a few percent.

Previous measurements [11,12] were done with $\mathrm{E}^{\star}_{\gamma} > 30$ MeV and $\theta^{\star}_{\gamma\mathrm{e}} > 20^0$. To compare with these measurements, we apply the same energy and angle requirements; the results are

$$\mathcal{R}_{\mathrm{Ke3}\gamma}(\mathrm{NA31\ 96; E}^{\star}_{\gamma} > 30\ \mathrm{MeV}, \theta^{\star}_{\gamma\mathrm{e}} > 20^0) = [0.934 \pm 0.066]\%, \quad (9)$$

$$\mathcal{R}_{\mathrm{Ke3}\gamma}(\mathrm{KTeV\ 01; E}^{\star}_{\gamma} > 30\ \mathrm{MeV}, \theta^{\star}_{\gamma\mathrm{e}} > 20^0) = [0.908 \pm 0.015]\%, \quad (10)$$

$$\mathcal{R}_{\mathrm{Ke3}\gamma}(\mathrm{KTeV\ 04; E}^{\star}_{\gamma} > 30\ \mathrm{MeV}, \theta^{\star}_{\gamma\mathrm{e}} > 20^0) = [0.916 \pm 0.017]\%, \quad (11)$$

and are consistent with each other. The current KTeV result is based on 4309 candidates, which is less than 1/3 of the KTeV 01 sample[9]. The loss in statistical precision is compensated by a significant reduction in the systematic uncertainty. The new analysis reported here (with $\mathrm{E}^{\star}_{\gamma} > 30$ MeV and $\theta^{\star}_{\gamma\mathrm{e}} > 20^0$) therefore has comparable precision with our earlier result, yet these two KTeV results are largely uncorrelated. The new KTeV result [Eq. (11)] supersedes the previous result [12] so that our radiative branching fractions are all based on the same analysis method. Figure 10(b) compares the measurements in Eqs. (9)–(11) with theory predictions. Table IV summarizes the $\mathcal{R}_{Ke3\gamma}$ results from KTeV and the predictions from KLOR.

[9]The $K_{e3\gamma}$ selection requirements for the KTeV 01 sample [12] were significantly more relaxed compared to the current analysis, and therefore resulted in higher statistics.

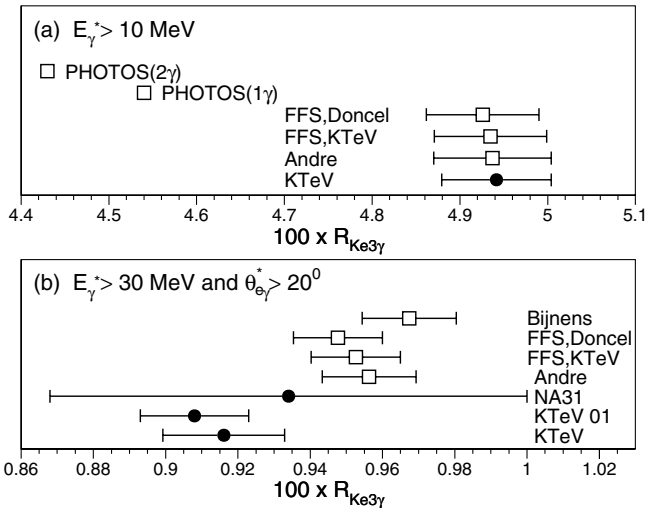

FIG. 10. Comparison of $\mathcal{R}_{Ke3\gamma}$ among experiment and theory for (a) $\mathrm{E}^{\star}_{\gamma} > 10$ MeV, and (b) $\mathrm{E}^{\star}_{\gamma} > 30$ MeV and $\theta^{\star}_{\gamma\mathrm{e}} > 20^0$. The experimental results are from KTeV (this result and also KTeV 01 [12]), and NA31 [11]. The theory predictions are from Andre [3], Fearing, Fischbach, and Smith, FFS [6], Bijnens [13], and PHOTOS [8]. The FFS prediction is determined by Doncel [14] and by KTeV, and each is corrected by $(1 + \delta^{e}_{K})^{-1}$ [3]. The theory uncertainties are taken to be $\delta^{e}_{K} = 0.013$ times the prediction. The PHOTOS predictions for one and two radiative photons are described in Sec. VI B.

C. Discussion

Our treatment of radiative effects propagates into the detector acceptance determination for the $K_L \to \pi^{\pm}\ell^{\mp}\nu$ branching fractions [4] and form factors [5]. The uncertainty in the acceptance from radiative effects is based on the agreement between our measurements of $\mathcal{R}_{\mathrm{K}\ell 3\gamma}$ and the predictions from KLOR [3]. Specifically, this uncertainty is taken to be the measurement-prediction difference, plus the quadrature sum of the experimental and theoretical uncertainties (from Tables III and IV).

For $\mathrm{K_L} \to \pi^{\pm}\mu^{\mp}\nu\gamma$, with $\mathrm{E}^{\star}_{\gamma} > 10$ MeV, the uncertainty in our treatment of radiative effects is evaluated to be 10.1%; with $\mathrm{E}^{\star}_{\gamma} > 30$ MeV, this uncertainty is 6.7%. For

TABLE IV. Summary of $\mathcal{R}_{Ke3\gamma}$ values measured by KTeV and predicted by KLOR.

Min $E^{\star}_{\gamma}$ (MeV)	Min $\theta^{\star}_{\gamma\mathrm{e}}$ (Degree)	KTeV Result (%)	KLOR Prediction (%)	KTeV/KLOR Ratio
10	0	4.942 ± 0.062	4.937 ± 0.067	1.001 ± 0.018
30	20	0.916 ± 0.017	0.956 ± 0.013	0.958 ± 0.022

$K_L \to \pi^\pm e^\mp \nu\gamma$, with $E^\star_\gamma > 10$ MeV, the corresponding uncertainty is 1.9%; with $E^\star_\gamma > 30$ MeV and $\theta^\star_{\gamma e} > 20^0$, the uncertainty is 6.4%. From these data-theory comparisons, which are all consistent, we assign the average uncertainty of 6% on KLOR's treatment of radiative effects.

The generated phase space distributions from KLOR are important in the form-factor measurements [5], and also in the $\mathcal{R}_{K\ell 3\gamma}$ measurements [Eq. (1)]. The KLOR generator is checked by comparing data and MC distributions for the photon energy ($E^\star_\gamma$) and for the angle between the photon and charged lepton ($\theta^\star_{\gamma\ell}$). Figs. 11 and 12 show these data-MC comparisons for $K_{\mu 3\gamma}$ and $K_{e3\gamma}$, respectively. Data and MC agree well in all cases, as indicated by the χ^2/dof. The data-MC comparison of the pion-photon angle (not shown) also agrees well for both radiative decay modes. The good quality of these data-MC comparisons shows that the KLOR generator is adequate for our experimental sensitivity.

VIII. CONCLUSION

For the radiative semileptonic decays $K_L \to \pi^\pm \mu^\mp \nu\gamma$ and $K_L \to \pi^\pm e^\mp \nu\gamma$, we have measured the branching fractions and the distributions of photon energy and photon-lepton angle (in the kaon center-of-mass frame). The results are consistent with predictions based on the KLOR program [3]. Our radiative branching fractions are also consistent with previous measurements [10–12], and with predictions based on the model of Fearing, Fischbach, and Smith [6].

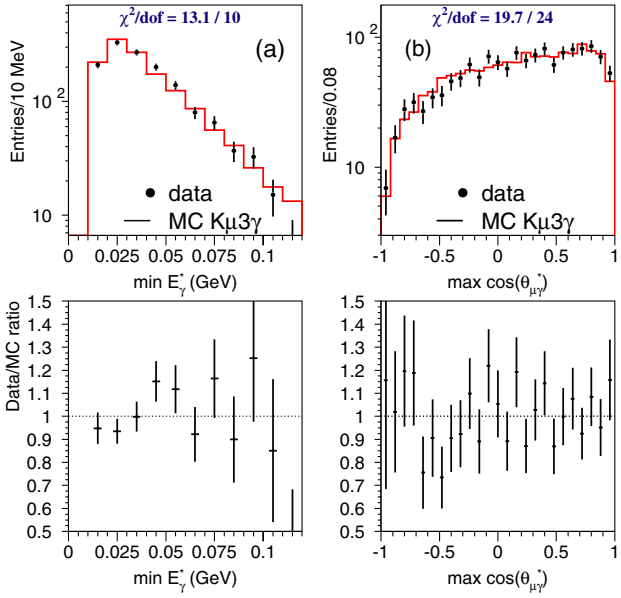

FIG. 11 (color online). Data-MC comparison of $K_{\mu 3\gamma}$ kinematics. For the two kaon energy solutions in the lab, (a) minimum radiated photon energy in kaon rest frame, and (b) maximum cosine of the photon-muon angle in kaon rest frame. Data are shown in dots; MC in histogram. The χ^2/dof at the top of each plot refers to the data-MC comparison; data/MC ratios are shown in the lower plots. All $K_{\mu 3\gamma}$ selection requirements have been applied, and background is subtracted.

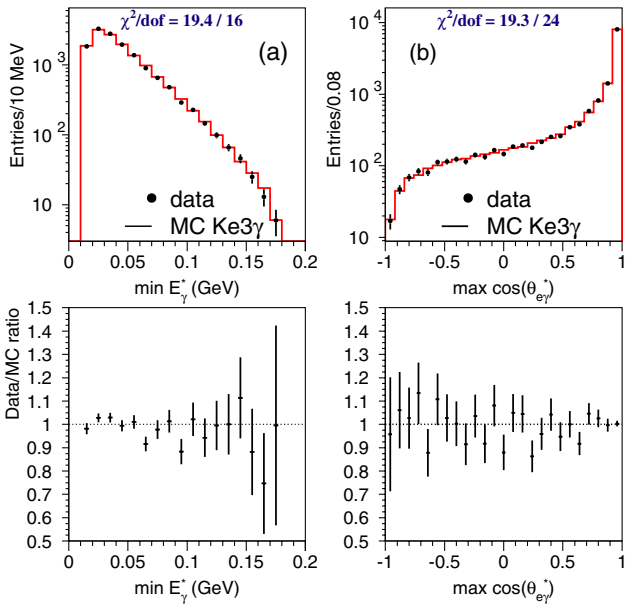

FIG. 12 (color online). Data-MC comparison of $K_{e3\gamma}$ kinematics. For the two kaon energy solutions in the lab, (a) minimum radiated photon energy in kaon rest frame, and (b) maximum cosine of the photon-electron angle in kaon rest frame. Data are shown in dots; MC in histogram. The χ^2/dof at the top of each plot refers to the data-MC comparison; data/MC ratios are shown in the lower plots. All $K_{e3\gamma}$ selection requirements have been applied.

APPENDIX A: EFFICIENCY OF THE PHOTON TRANSVERSE PROFILE REQUIREMENT

The transverse profile for energy deposits in the CsI calorimeter is based on the energy distribution in the crystals that are used to determine the cluster energy. A CsI cluster uses 49 small crystals ($2.5 \times 2.5 \times 50$ cm^3) or nine large crystals ($5.0 \times 5.0 \times 50$ cm^3). To determine the photon likelihood for a cluster, we use a shape-χ^2_γ variable,

$$\text{shape}\text{–}\chi^2_\gamma \equiv \sum_{i=1}^{N} \frac{(f_i^{\text{data}} - \bar{f}_i)^2}{\text{RMS}_i^2}, \qquad \text{(A1)}$$

where f_i^{data} is the fraction of energy in the i'th crystal, $\bar{f}_i$ is the position-dependent average energy fraction in the i'th crystal as measured in $K_L \to \pi^0\pi^0$ decays, and RMS_i is the measured RMS of $\bar{f}_i$. To reduce background in the $K_{\ell 3\gamma}$ analyses, we require shape–$\chi^2_\gamma < 10$, a considerably stricter requirement than used in our other analyses involving $K_L \to \pi^0\pi^0$ and $K_L \to \pi^0\pi^0\pi^0$ decays [4,9].

In the $K_L \to \pi^\pm e^\mp \nu\gamma$ analysis, the inefficiency of the shape-χ^2_γ requirement for photons is 2.0% as determined from MC. Most of the loss is from soft external brems-

strahlung photons that overlap the radiated photon. Contributions to the shape-χ^2_γ tail are understood with 10% precision, resulting in 0.2% uncertainty on $\mathcal{R}_{Ke3\gamma}$. For $K_L \to \pi^\pm \mu^\mp \nu\gamma$, the photon inefficiency is 0.6%, resulting in a 0.06% uncertainty in $\mathcal{R}_{K\mu3\gamma}$.

As a crosscheck in the $K_L \to \pi^\pm e^\mp \nu\gamma$ analysis, we consider a stricter requirement of shape–$\chi^2_\gamma < 3$; the additional loss is $(5.6 \pm 0.2)\%$ in data, and $(5.8 \pm 0.1)\%$ in MC.

APPENDIX B: SEARCH FOR $K_L \to \pi^0\pi^\pm\mu^\mp\nu$

The search for $K_L \to \pi^0\pi^\pm\mu^\mp\nu$ decays uses the same data sample as the $\mathcal{R}_{K\mu3\gamma}$ analysis. A pion and muon track are searched using the two-track analysis described in Sec. IV A. To increase the acceptance, requirements on the decay vertex and kaon energy are relaxed. Next, we search for two photons in the CsI calorimeter such that the two-photon invariant mass is consistent with the π^0 mass. This sample of "$\pi^0\pi^\pm\mu^\mp$" candidates is mainly background from $K_L \to \pi^+\pi^-\pi^0$ decays in which one of the pions decays into a muon plus neutrino. To reduce this background, the muon-neutrino invariant mass ($m_{\mu\nu}$) is computed for both kaon energy solutions, and both $m_{\mu\nu}$ solutions are required to be well away from the charged pion mass. A $K_L \to \pi^0\pi^\pm\mu^\mp\nu$ candidate is defined such that the $m_{\mu\nu}$ solution closest to the pion mass ($m'_{\mu\nu}$) is between 170 and 210 MeV/c^2. Figure 13(a) shows the $m'_{\mu\nu}$ distribution; the data are shown as dots, and $K_L \to \pi^+\pi^-\pi^0$ MC is shown by the histogram. For data, there are no events in the signal region; the background prediction from $K_L \to \pi^+\pi^-\pi^0$ MC describes the data well.

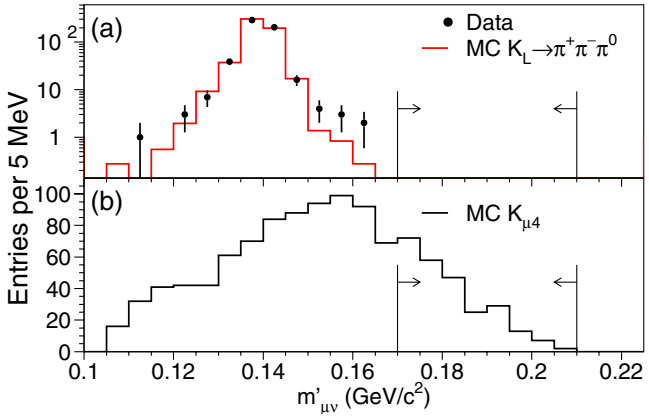

FIG. 13 (color online). For the two kaon energy solutions, the invariant muon-neutrino mass closest to pion mass ($m'_{\mu\nu}$) is shown in (a) for data (dots) and MC $K_L \to \pi^+\pi^-\pi^0$ (histogram). (b) shows the $m'_{\mu\nu}$ distribution for MC $K_L \to \pi^0\pi^\pm\mu^\mp\nu$. The vertical lines show the selection window for $K_L \to \pi^0\pi^\pm\mu^\mp\nu$ candidates. All $K_L \to \pi^0\pi^\pm\mu^\mp\nu$ selection requirements, except for $m'_{\mu\nu}$, have been applied.

Figure 13(b) shows the $m'_{\mu\nu}$ distribution for $K_L \to \pi^0\pi^\pm\mu^\mp\nu$ MC. From this MC sample, the acceptance is determined to be 0.25%. For the normalization mode, there are 1.86×10^6 $K_L \to \pi^\pm\mu^\mp\nu$ candidates, and the acceptance (from MC) is 13.4%. The resulting upper limit is

$$B(K_L \to \pi^0\pi^\pm\mu^\mp\nu) < 2 \times 10^{-5} \quad (90\% \text{ confidence}). \tag{B1}$$

APPENDIX C: MEASUREMENT OF FAKE-PHOTON PROBABILITY FROM PION INTERACTIONS

A potential background for $K_{\ell3\gamma}$ is a nonradiative $K_{\ell3}$ decay in which the pion interacts hadronically in the material upstream of the CsI and generates a CsI cluster that satisfies the photon identification cuts. In this appendix, we first describe how this effect is simulated, and then use $K_{L,S} \to \pi^+\pi^-$ events to measure the fake-photon probability in both the data and simulation.

The effects of π-hadron interactions are simulated with a GEANT-based library that stores hadronic secondaries produced from pion interactions. When a charged pion is traced through the detector in the KTeV MC, the hadronic interaction probability is computed for each detector element. To simulate a π-hadron interaction, a shower is selected from the GEANT library based on the pion momentum, and the secondaries are traced through the detector.

To check the simulation of hadronic showers, we measure the fake-photon probability for $K_{L,S} \to \pi^+\pi^-$ decays. This decay mode is ideal because simple kinematic cuts (see below) remove events with radiative photons, and therefore any extra cluster in the CsI calorimeter must be from a hadronic interaction. To have sufficient statistics, we use the $\pi^+\pi^-$ sample from the Re(ϵ'/ϵ) analysis [9]. For this data sample, a regenerator placed in one of the beams was used to generate K_S; $K_{L,S} \to \pi^+\pi^-$ decays from both beams are used in this study. The regenerator veto is used to suppress accidental photon clusters arising from interactions of the neutral beam in the regenerator. Very tight requirements are made on the $\pi^+\pi^-$ invariant mass (495–502 MeV/c^2) and transverse momentum ($p_t^2 < 10^{-4}$ GeV$^2/c^2$) to ensure that photons from radiative $K_{L,S} \to \pi^+\pi^-\gamma$ are well below the 3 GeV cluster-energy requirement.

To remove events in which both pions undergo a hadronic shower, one of the pions is required to deposit energy in only one CsI crystal (compared with 49 crystals used to sum energy for photon showers), and no other cluster is allowed to lie within 30 cm of this "nonshower cluster." The probability for a pion to satisfy this nonshower requirement is 10%; the event is rejected if both pions satisfy the nonshower requirement. Finally, to reduce accidentals,

the regenerator veto is applied during a 150 ns window (8 RF buckets) centered on the event start time.

After the selection criteria described above, there are 4.7×10^6 $K_{L,S} \to \pi^+\pi^-$ candidates. Using this sample, photon cluster candidates are searched for using the same criteria as in the $K_{\ell 3\gamma}$ analysis. Figure 14(a) shows the π-cluster separation at the CsI calorimeter; the enhancement below 40 cm is from π-hadron interactions. After the 40 cm π-cluster separation requirement, Fig. 14(b) shows the energy distribution for CsI clusters that satisfy the $K_{\ell 3\gamma}$ photon requirements. The MC prediction is also shown after normalizing the MC to have the same number of $K_{L,S} \to \pi^+\pi^-$ events as the data. Since 98% of the photon clusters above 6 GeV are from accidentals (dashed histogram in Fig. 14(b)), this analysis uses photon cluster candidates with energy between three and 6 GeV. With this additional cluster-energy requirement, the fraction of $K_{L,S} \to \pi^+\pi^-$ candidates satisfying the $K_{\ell 3\gamma}$ photon requirements is $(7.62 \pm 0.40) \times 10^{-5}$ in data, and $(8.06 \pm 0.29) \times 10^{-5}$ in MC. According to the MC, 60% of the events with extra clusters are due to accidental activity and the remaining 40% is from pion interactions upstream of the CsI. Note that the effect of accidentals is more significant in this $K_{L,S} \to \pi^+\pi^-$ sample because the beam intensity is much higher compared to the sample used to measure $\mathcal{R}_{K\ell 3\gamma}$. Assuming no uncertainty in the accidental contribution for $K_{L,S} \to \pi^+\pi^-$, the relative error on the contribution from π-hadron interactions is 20%.

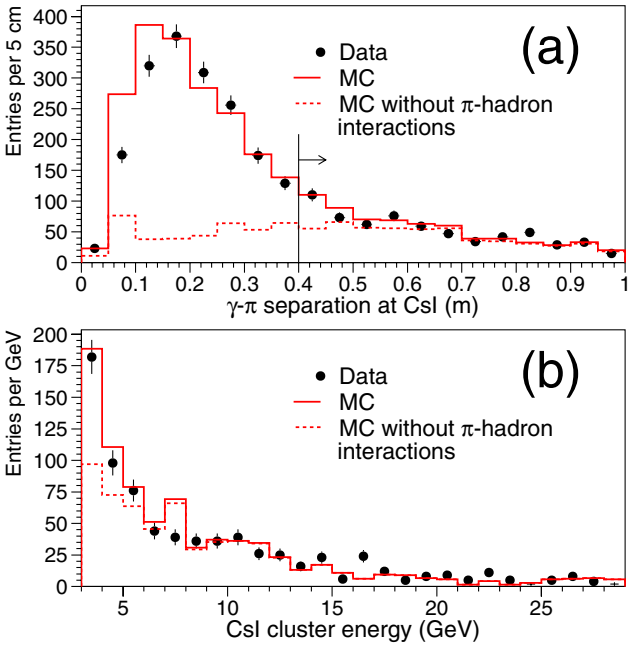

FIG. 14 (color online). For reconstructed $K_{L,S} \to \pi^+\pi^-$ decays with an extra cluster that satisfies the $K_{\ell 3\gamma}$ photon identification requirements, (a) π–γ separation at CsI (with separation cut removed) and (b) photon energy distribution. Samples shown are data (dots), MC (histogram), and MC without π-hadron interactions (dashed histogram). The MC is normalized to the total number of $K_{L,S} \to \pi^+\pi^-$ candidates.

[1] KTeV Collaboration, T. Alexopoulos *et al.*, Phys. Rev. Lett. **93**, 181802 (2004).
[2] W. Marciano and A. Sirlin, Phys. Rev. Lett. **56**, 22 (1986).
[3] T. Andre (2004), hep-ph/0406006.
[4] KTeV Collaboration, T. Alexopoulos *et al.*, Phys. Rev. D **70**, 092006 (2004).
[5] KTeV Collaboration, T. Alexopoulos *et al.*, Phys. Rev. D **70**, 092007 (2004).
[6] H. Fearing *et al.*, Phys. Rev. D **2**, 542 (1970).
[7] E. S. Ginsberg, Phys. Rev. D **1**, 229 (1970).
[8] E. Barberio and Z. Was, Comput. Phys. Commun. **79**, 291 (1994).
[9] KTeV Collaboration, A. Alavi-Harati *et al.*, Phys. Rev. D **67**, 012005 (2003).
[10] NA48 Collaboration, Bender *et al.*, Phys. Lett. B **418**, 411 (1998).
[11] NA31 Collaboration, Leber *et al.*, Phys. Lett. B **369**, 69 (1996).
[12] KTeV Collaboration, A. Alavi-Harati *et al.*, Phys. Rev. D **64**, 112004 (2001).
[13] J. Bijnens, Nucl. Phys. **B396**, 81 (1993).
[14] M. G. Doncel, Phys. Lett. B **32**, 623 (1970).